Chapter 1
Thin Films of Bismuth-Telluride-Based Alloys

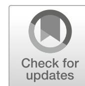

Masayuki Takashiri

1.1 Introduction

Thin films of bismuth telluride (Bi_2Te_3), antimony telluride (Sb_2Te_3), and bismuth selenide (Bi_2Se_3) are expected to be useful as miniaturized thermoelectric power generators in energy-constrained embedded systems owing to their excellent electrical and thermal properties near 300 K [1–4]. Their alloys have rhombohedral tetradymite-type crystal structures with the space group $D_{3d}^5\left(R\overline{3}m\right)$ and hexagonal unit cells [5]. As an example, the crystal structure of Bi_2Te_3 is described in Fig. 1.1. The unit cell is composed of five covalently bonded monatomic sheets along the *c*-axis in the sequence $–Te^{(1)}–Bi–Te^{(2)}–Bi–Te^{(1)}–$. The superscripts (1) and (2) denote two different chemical states of the anions. The bonds between $Te^{(1)}$ and Bi include both covalent and ionic bonds, while $Te^{(2)}$ and Bi are purely bonded by a covalent bond. A very weak van der Waals attraction exists between neighboring $Te^{(1)}$ layers. The crystal structures of Sb_2Te_3 and Bi_2Se_3 are equal to that of Bi_2Te_3, but their lattice parameters are different, as presented in Table 1.1 [6]. The lattice parameter along the *c*-axis is approximately 7 times larger than that along the *a*- or *b*-axis, which contributes to the material's remarkable anisotropic thermoelectric properties [7–10]. The maximum electrical conductivity is approximately 10^3 S/cm. The electrical conductivity along the *a*,*b*-plane is approximately three times larger than that along the *c*-axis [6]. The lattice thermal conductivity along the *a*,*b*-plane (1.5 W/(m·K)) is approximately two times larger than that along the *c*-axis (0.7 W/(m·K)) [11]. The Seebeck coefficient of Bi_2Te_3 almost does not exhibit anisotropy [7]. The Seebeck coefficient varies from −200 to 200 μV/K upon addition of acceptor or donor impurities. In order to reduce the lattice thermal

M. Takashiri (✉)
Department of Materials Science, Tokai University, Hiratsuka, Kanagawa, Japan
e-mail: takashiri@tokai-u.jp

© Springer Nature Switzerland AG 2019
P. Mele et al. (eds.), *Thermoelectric Thin Films*,
https://doi.org/10.1007/978-3-030-20043-5_1

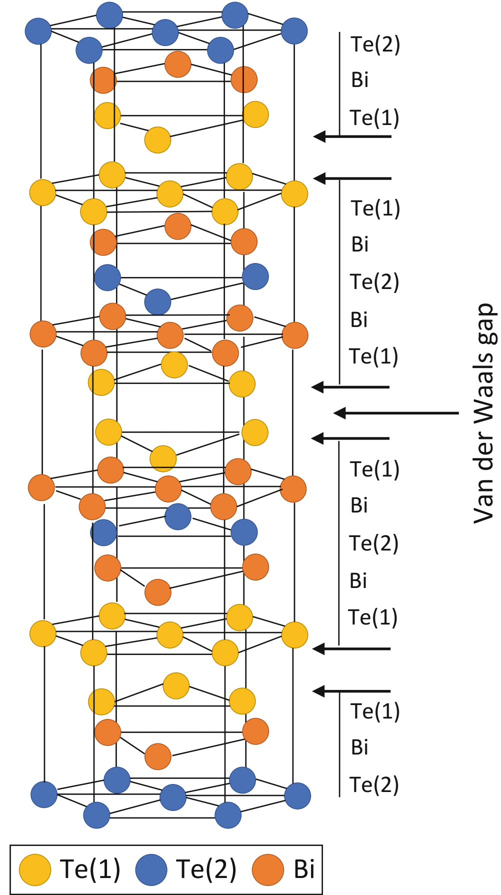

Fig. 1.1 Schematic crystal structure of Bi_2Te_3

Table 1.1 Lattice constants and bandgaps of Bi_2Te_3-based materials [6]

	Lattice constant		
	a,*b*-axis	*c*-axis	Band gap
	Å	Å	eV
Bi_2Te_3	4.35	30.3	0.13
Sb_2Te_3	4.25	30.3	0.22
Bi_2Se_3	4.14	28.6	0.12

conductivity, ternary alloys such as $(Bi_{1-x}Sb_x)_2Te_3$ and $Bi_2(Se_{1-x}Te_x)_3$ are prepared [12, 13]. $(Bi_{1-x}Sb_x)_2Te_3$ is formed by replacing Sb atoms with Bi atoms, and exhibits a p-type conduction behavior. On the other hand, $Bi_2(Se_{1-x}Te_x)_3$ is formed by replacing Se atoms mainly with $Te^{(2)}$ atoms, and exhibits an n-type conduction behavior.

Figure 1.2 shows the band structure of Bi_2Te_3 determined by a first-principle calculation [14]. It should be noted that Bi_2Se_3, Sb_2Te_3, and ternary alloys exhibit similar band structures [15–17]. Even though the band structure slightly changes

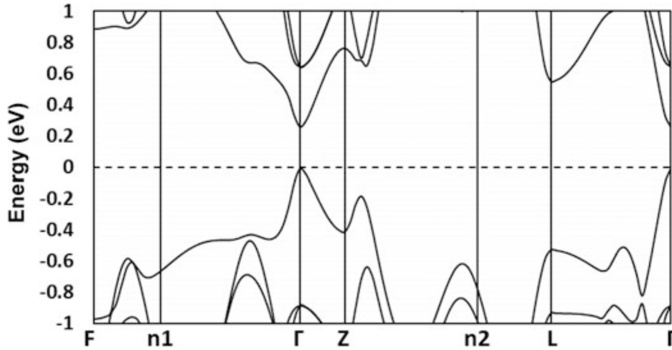

Fig. 1.2 Band structure of Bi_2Te_3

with the calculation parameters, Bi_2Te_3 exhibits properties of an indirect-transition-type semiconductor with a band gap of 0.1–0.2 eV. Its complex crystal structure yields a valence band maximum in the middle of the Z–F direction and conduction band minimum in the middle of the Γ–Z or Z–F direction. Upon carrier doping, Bi_2Te_3 exhibits a multi-valley structure.

1.2 Thin-Film Deposition Methods

1.2.1 Conventional Deposition Methods for Bi_2Te_3-Based Alloy Thin Films

Various film deposition methods including sputtering [18–20], vacuum evaporation [21–24], electrodeposition [25–28], drop-casting [29–32], pulsed laser deposition [33–36], metal organic chemical vapor deposition (MOCVD) [37–39], and molecular beam epitaxy (MBE) [40–42] have been used to deposit Bi_2Te_3-based alloy thin films. As mentioned above, the advantages of the thin-film technology are the reductions in device size and manufacturing cost by incorporating nanoscale effects. Among the various film deposition methods, sputtering, electrodeposition, and printing are the most favorable to realize the advantages of the film deposition. Therefore, we introduce these three deposition methods in this section.

1.2.2 Sputtering Deposition Method

In sputtering, high-energy particles are incident on a target material; they remove constituent atoms of the target from its surface, which are then deposited as a thin film on a substrate. Generally, the sputtering deposition methods are divided

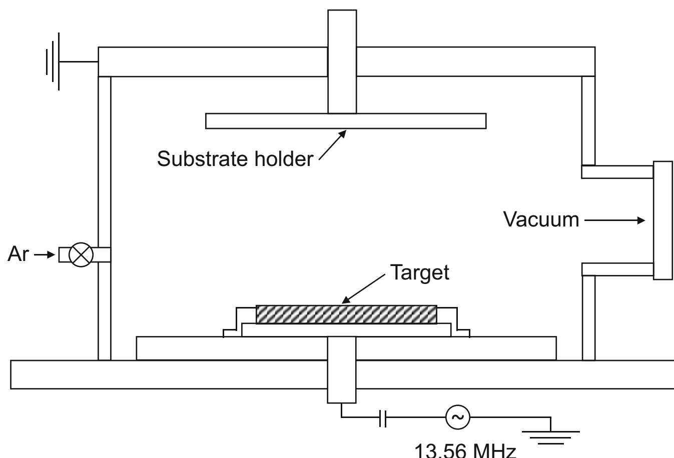

Fig. 1.3 Schematic diagram of the RF magnetron sputtering system

into direct-current (DC) sputtering and radio-frequency (RF) sputtering. The compartments in the vacuum chamber of both DC and RF sputtering are basically the same. The difference is the application of a DC or RF power between the substrate and target to generate the plasma. One of the advantages of the RF sputtering is the ability to use insulator targets and deposit insulating films and conductive oxide films. In addition, to increase the deposition rate and decrease the thin film damage due to high-energy anion impacts, a magnetic field is introduced into the RF sputtering. Figure 1.3 shows a schematic diagram of the RF magnetron sputtering equipment. By installing a permanent magnet on the back of the target, a parallel leakage magnetic field from the target surface to the center is generated. Owing to the parallel magnetic field on the front face of the target, the secondary electrons emitted from the target surface drift on the target owing to the Lorentz force, enabling to efficiently organize the ionization effect even at a low discharge gas pressure. Therefore, an improvement in deposition rate by a high-current-density discharge could be achieved. In addition, to further improve the thermoelectric performance, one approach is to increase the electrical conductivity through an increase in the number of charge carriers in the films by adding H_2 gas during the sputtering (in general, pure Ar gas atmospheres are used) [43–46]. It has been reported that the electrical conductivities of transparent conducting oxide (TCO) films, including indium tin oxide (ITO) and doped zinc oxide (ZnO), increased with the introduction of H_2 gas.

We present typical Bi_2Te_3 thin films prepared using RF magnetron sputtering with the introduction of H_2 gas [47]. The surface morphologies analyzed by scanning electron microscope (SEM) of Bi_2Te_3 thin films with different mixing ratios are shown in Fig. 1.4. The surface morphologies of the thin films were strongly dependent on the mixing ratio. The thin film prepared with pure Ar had a relatively rough surface with densely arranged irregular crystal grains with sharp

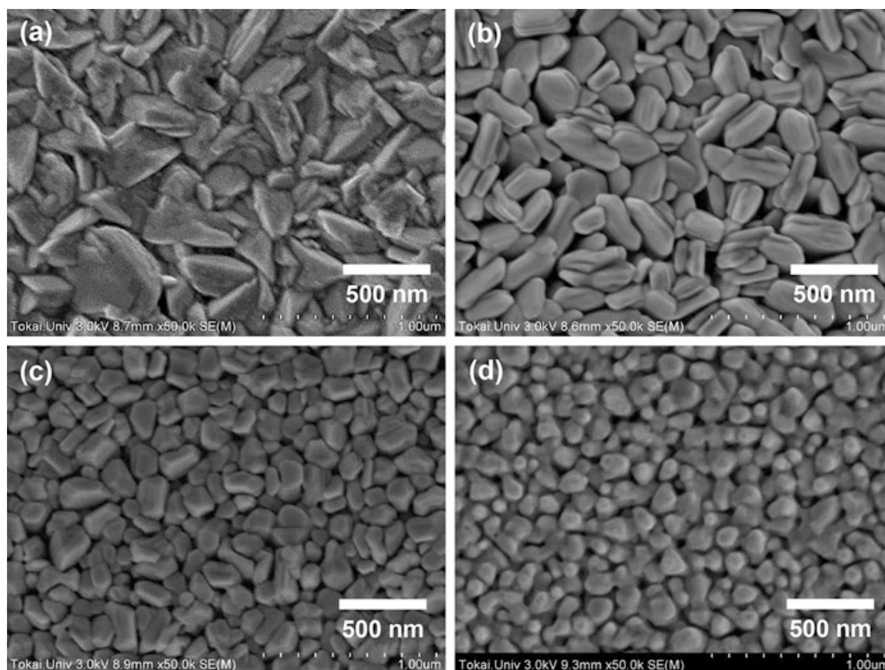

Fig. 1.4 SEM images showing the surface morphologies of the Bi_2Te_3 thin films. (**a–d**) Surface morphologies of the samples with $H_2/(H_2 + Ar)$ mixing ratios of 0%, 5%, 10%, and 15%, respectively [47]

edges (Fig. 1.4a). At a mixing ratio of 5% (Fig. 1.4b), hexagonal plate-like crystal grains with a plate thickness of ~300 nm and diameter of ~100 nm were randomly arranged, and voids were observed between the grains. When the mixing ratio was further increased to 10% (Fig. 1.4c), isotropic granular grains with sizes of ~100 nm were densely arranged. The increase in the mixing ratio to 15% (Fig. 1.4d) yielded slightly smaller rounded crystal grains, compared to those observed for the mixing ratio of 10%; the sizes of the voids between the grains slightly increased. These changes in surface morphology implied that surface atoms, particularly those located at the edges of the grains, evaporated when the proportion of H_2 gas increased.

Figure 1.5 shows the atomic compositions of the thin films with different $H_2/(H_2 + Ar)$ ratios, determined by electron probe microanalyzer (EPMA). The atomic concentrations of tellurium and bismuth varied with the mixing ratio. The samples with mixing ratios of 0%, 5%, and 10% exhibited approximately stoichiometric proportions. However, when the mixing ratio increased to 15%, the concentration of bismuth increased, while that of tellurium decreased. The atomic composition was: Bi: 56 at.% and Te: 44 at.%, which significantly deviated from the stoichiometric proportion (Bi: 40 at.% and Te: 60 at.%). Considering both deposition rate and atomic composition, Te atoms were mainly evaporated from the

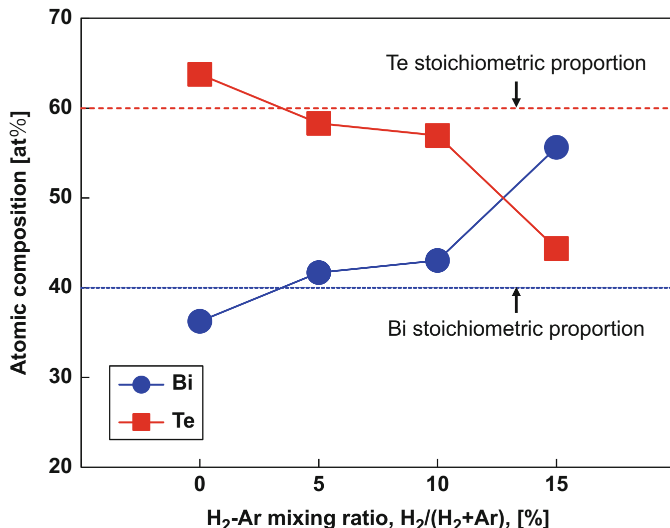

Fig. 1.5 Atomic concentrations of bismuth and tellurium as a function of the $H_2/(H_2 + Ar)$ mixing ratio [47]

film surface by a chemical reaction with hydrogen, producing hydrogen telluride [48, 49].

Figure 1.6 shows relationships between $H_2/(H_2 + Ar)$ and in-plane thermoelectric properties of the Bi_2Te_3 thin films. The Seebeck coefficient was significantly influenced by the proportion of H_2 gas, as shown in Fig. 1.6a. The Seebeck coefficient of the Bi_2Te_3 thin film at a mixing ratio of 0% was −126 μV/K; when the mixing ratio was increased, the absolute value decreased. In particular, the Seebeck coefficient significantly decreased at a mixing ratio of 15%, as the atomic concentrations of Bi and Te considerably deviated from the stoichiometric proportions of Bi_2Te_3, and thus, the BiTe phase appeared [50]. Figure 1.6b shows that the electrical conductivities of the Bi_2Te_3 thin films prepared with the mixing ratios of 0% and 5% were 351 and 429 S/cm, respectively. The latter value was not the highest value of all of the samples even though this thin film had the largest crystallite size and highest degree of crystal orientation, possibly owing to the appearance of voids between the grains and oxygen concentration inside the film higher than those inside the films prepared at the mixing ratios of 10% and 15%. For the mixing ratio of 10%, the electrical conductivity increased to 741 S/cm. This increase was thought to be determined by two factors. The first factor was a reduction in the oxygen concentration inside the thin film contributing to an increase in mobility or suppression of the decrease in mobility due to the lower crystal orientation [51]. The other factor was the appearance of Te vacancies acting as donors, leading to an increase in the carrier concentration [52, 53]. We considered that the appearance of the Te vacancies contributes more than the reduction in the

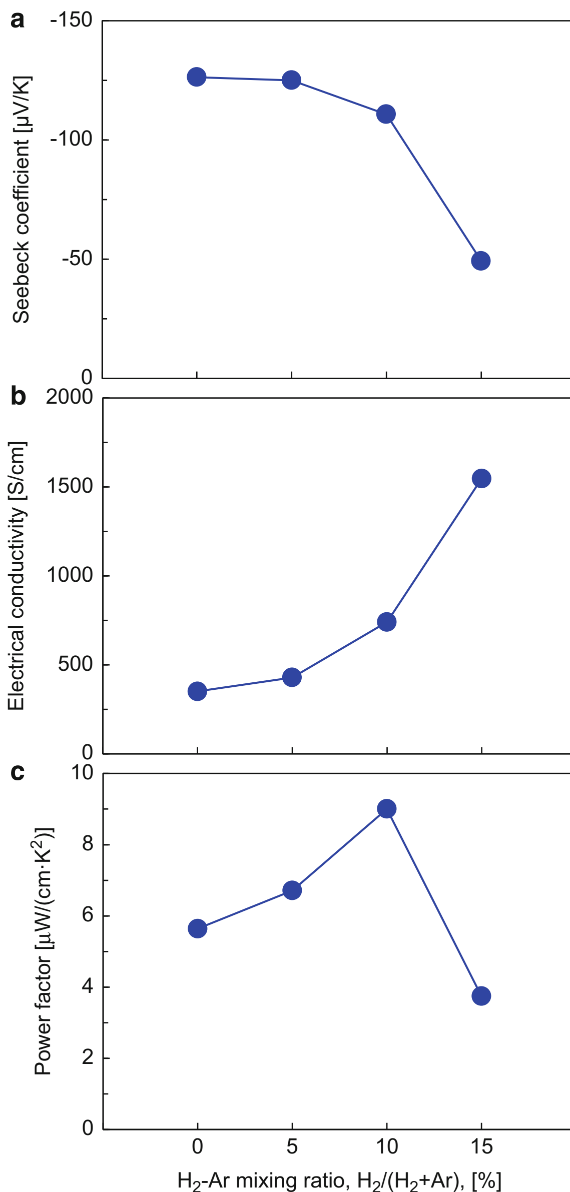

Fig. 1.6 (**a**) Seebeck coefficients, (**b**) electrical conductivities, and (**c**) power factors of the Bi_2Te_3 thin films as a function of the $H_2/(H_2 + Ar)$ mixing ratio [47]

oxygen concentration, as the variation in the content of tellurium is larger than that of oxygen. An excessive thermal annealing has caused a similar phenomenon [54, 55]. When the mixing ratio was further increased, the electrical conductivity significantly increased. The thin film prepared at a mixing ratio of 15% exhibited the highest electrical conductivity of 1547 S/cm, even though it exhibited the

smallest crystallite size and voids between the grains. This phenomenon can also be explained by the appearance of the BiTe phase [50]. The power factor as a function of the H_2:Ar mixing ratio is shown in Fig. 1.6c. The power factor of the thin film at the mixing ratio of 0% was relatively low, 5.6 μW/(cm·K^2), which was attributed to the lower electrical conductivity owing to the smaller crystallite size and higher oxygen concentration, despite the relatively high Seebeck coefficient. The power factor increased with the mixing ratio. At the mixing ratio of 10%, the power factor reached the highest value of 9.0 μW/(cm·K^2), owing to the relatively high electrical conductivity and Seebeck coefficient. When the mixing ratio was 15%, the power factor was significantly decreased owing to the decrease in the Seebeck coefficient. Therefore, a moderate mixing ratio (10%) of H_2 gas promoted a low oxygen concentration in the thin film without causing voids, leading to the higher electrical conductivity and power factor.

1.2.3 Electrodeposition Methods

The electrodeposition method is one of the wet processes in a solution phase. There are mainly two types of electrodepositions: electrolytic and non-electrolytic platings. The electrodeposition method generally has advantages such as a lower cost, compared with the dry process techniques. In addition, the electrodeposition is a low-temperature process below 80 °C. Another advantage of the electrodeposition is the high deposition rate, which enables to deposit a thick film in a short time. Regarding the Bi_2Te_3-based alloy thin films, the electrolytic plating has been used since Takahashi et al. electrodeposited Bi_2Te_3-based alloy films for the first time in the 1990s [56]. Figure 1.7 presents a schematic diagram of the electrolytic plating method. The thin films are generally prepared using a standard three-electrode cell system, with working, counter, and reference electrodes inserted in an electrolyte solution. The thin film is deposited on the working electrode when a constant voltage (potentiostatic electrodeposition) or constant current density (galvanostatic electrodeposition) is applied between the working and counter electrodes.

We present typical Sb_2Te_3 thin films prepared using potentiostatic electrodepositions [57]. In order to increase the film crystallinities, thermal annealing at different temperatures was performed. The SEM images in Fig. 1.8 show that the surface morphologies of the electrodeposited Sb_2Te_3 films are strongly affected by the annealing temperature. Figure 1.8a shows that the as-deposited film is covered with approximately spherical grains of a smooth surface; the grain size is approximately 1 μm. When the thin film is annealed at 200 °C, the shape of the grains remains unchanged, but the grain size increases to approximately 2 μm (Fig. 1.8b). The grain shape and size of the thin film annealed at 250 °C are almost the same as those of the thin film annealed at 200 °C (Fig. 1.8c). At an annealing temperature of 300 °C, the grain size remains unchanged from that of the thin film at 250 °C, but the grain surface becomes confetti-like (Fig. 1.8d). The surface of the thin film annealed at 350 °C seems to have needle-shaped crystals growing on the spherical

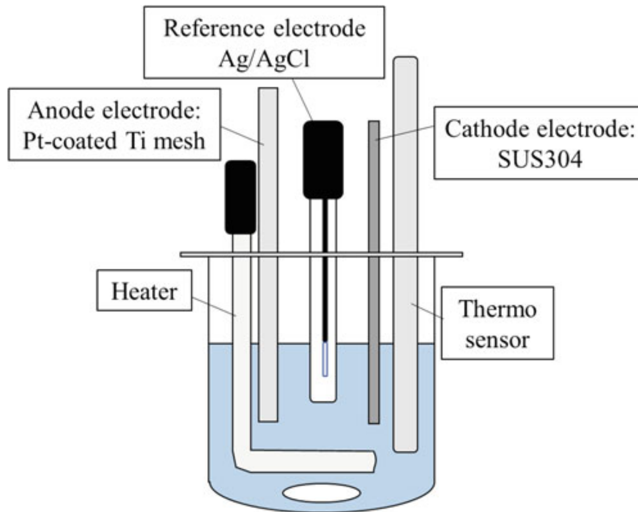

Fig. 1.7 Schematic diagram of the electrodeposition system

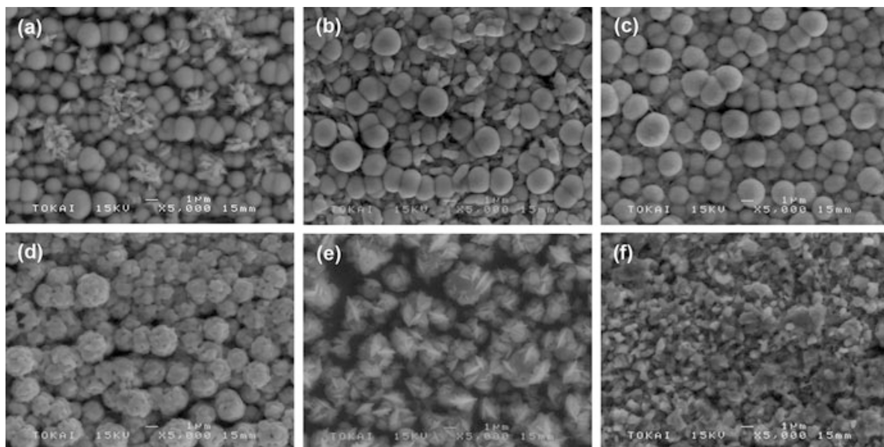

Fig. 1.8 SEM images of the surface morphologies and grain structures of the Sb_2Te_3 thin films annealed at (**a**) room temperature (as-deposited), (**b**) 200, (**c**) 250, (**d**) 300, (**e**) 350, and (**f**) 400 °C [57]

grains, with an increased space between grains (Fig. 1.8e). Furthermore, when the annealing temperature increases to 400 °C, the surface morphology significantly changes (Fig. 1.8f). The thin film exhibits a porous structure with irregularly shaped submicron grains.

The dependence of the atomic composition on the annealing temperature and impurities originated from the SUS304 stainless-steel substrate (Fe:Cr:Ni = 70:19:9) is shown in Fig. 1.9. It should be noted that the EMPA

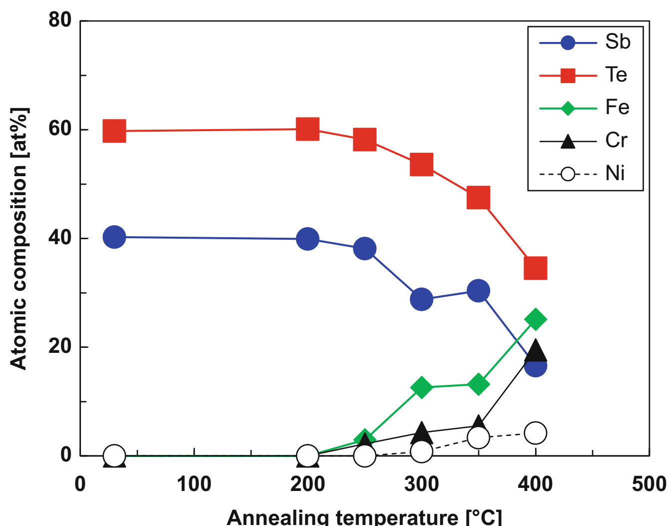

Fig. 1.9 Annealing temperature dependences of the atomic compositions of the Sb_2Te_3 thin films, determined by EPMA [57]

measurement was performed after the thin films were removed from the substrates. The as-deposited thin-film data are plotted at 27 °C. The as-deposited film and the film annealed at 200 °C exhibit the stoichiometric atomic composition (Sb:Te = 40:60); no contamination from the substrate is observed. When the annealing temperature is increased to 250 °C, the atomic concentrations of tellurium and antimony decreased, and small amounts of iron and chromium can be observed. This indicates that the elements in the substrate gradually diffuse into the Sb_2Te_3 thin film upon the increase in the annealing temperature. With the further increase in the annealing temperature to 300 °C, the atomic concentrations of tellurium and antimony continue to decrease, and Fe, Cr, and Ni impurities are detected. In particular, the atomic concentration of Fe reaches approximately 13 at.%. Finally, the thin film annealed at 400 °C has a significantly increased of impurities. The total atomic concentration of impurities from the substrate reaches approximately 50 at.%.

Figure 1.10 shows relationships between the annealing temperature and in-plane thermoelectric properties of the Sb_2Te_3 thin films. In Fig. 1.10a, the as-deposited thin film and thin film annealed at 200 °C with relatively high Seebeck coefficients of approximately 170 μV/K. In general, antimony telluride alloys exhibit high Seebeck coefficients at their stoichiometric atomic compositions. With the increase in the annealing temperature, the Seebeck coefficient decreases. The Seebeck coefficient of the thin film annealed at 350 °C is 66 μV/K. At the annealing temperature of 400 °C, the Seebeck coefficient −37 μV/K, indicating that the thin film has become an n-type semiconducting material, as the Sb_2Te_3 crystal structure does not exist in the thin film at this annealing temperature. In Fig. 1.10b, the

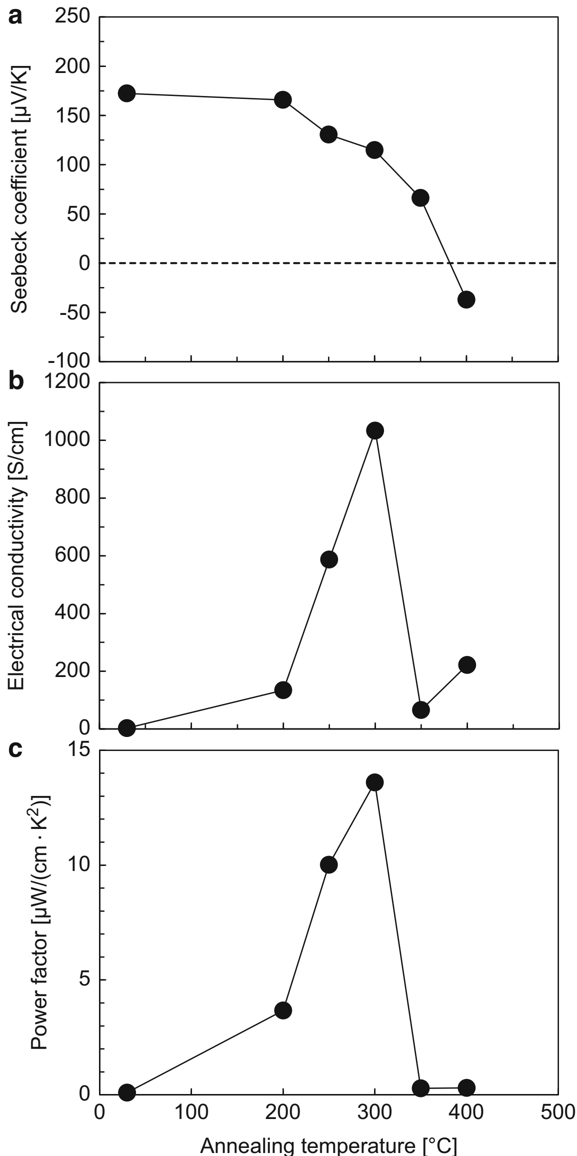

Fig. 1.10 Annealing temperature dependences of the (**a**) Seebeck coefficients, (**b**) electrical conductivities, and (**c**) power factors of the Sb_2Te_3 thin films [57]

as-deposited thin film exhibits a very low electrical conductivity, possibly as this film has a lower mobility owing to the low crystallinity and small crystallite size, whereas the carrier concentration is suitable leading to the high Seebeck coefficient. The electrical conductivity rapidly increases between the annealing temperatures of 200 and 300 °C. The thin film annealed at 300 °C exhibits the maximum electrical conductivity of 1034 S/cm. The rapid increase in the electrical conductivity is due to

the crystallinity improvement and increase in the carrier concentration induced by the impurity contamination. At the annealing temperature of 350 °C, the electrical conductivity rapidly decreases, possibly as the gaps between the grains increase, as shown in Fig. 1.9e. The lowest electrical conductivity is observed for the thin film annealed at 400 °C owing to its porous structure, as shown in Fig. 1.9f. We calculated the power factor using the measured Seebeck coefficient and electrical conductivity, as shown in Fig. 1.10c. The dependence of the power factor on the annealing temperature has a similar trend as that of the electrical conductivity. We obtain antimony telluride thin films with higher thermoelectric performances at the annealing temperatures of 250 and 300 °C. The thin film annealed at 300 °C exhibits the maximum power factor of 13.6 $\mu W/(cm \cdot K^2)$. As mentioned above, the thin film annealed at 300 °C contains a certain amount of impurities from the substrate. The impurities contribute to the decrease in the Seebeck coefficient as well as to the increase in the electrical conductivity. The contribution to the increase in the electrical conductivity surpasses that to the decrease in the Seebeck coefficient.

1.2.4 Combination Method of Sputtering and Electrodeposition

As mentioned above, electrodeposition is one of the most favorable methods as it is very cost-effective owing to its simple scalability and low operating temperature without the requirement for vacuum conditions. However, one of the drawbacks of electrodeposition is that films are deposited only on conductive electrodes. Therefore, to measure their thermoelectric properties or fabricate thermoelectric devices, the films should be transferred from conductive to insulating substrates using resin adhesives. During this transfer, micropores appear in the films, hindering their electrical conductions. Therefore, a method that can suppress the micropores in the films should be developed. A possible method is to electrochemically deposit the films on seed layers, thus generating films with the same compositions as those of the electrodeposited films using a dry process such as sputtering on insulating substrates [58]. The thermoelectric properties of these electrodeposited films can be measured without the transfer process. Furthermore, this method is expected to promote the crystal growth of electrodeposited films owing to the formation of a homogeneous interface.

We present typical as-grown Bi_2Te_3 electrodeposited films using sputtered Bi_2Te_3 seed layers (AES films). Figure 1.11 shows the SEM surface and cross-section morphologies of a typical AES film. Figure 1.11a shows that the AES film is composed of nanoscale (smaller than 0.5 μm) crystal grains with a densified morphology and smooth and homogeneous surface. A cross-section image of the AES film is shown in Fig. 1.11b. The interface between the electrodeposited film and seed layer is clearly observed; no voids are observed. The grain size of the electrodeposited film was larger than that of the seed layer. The measured thicknesses of the electrodeposited film and seed layer were 1.6 and 1.3 μm, respectively. For comparison, we analyzed the surface morphologies of the standard electrodeposited

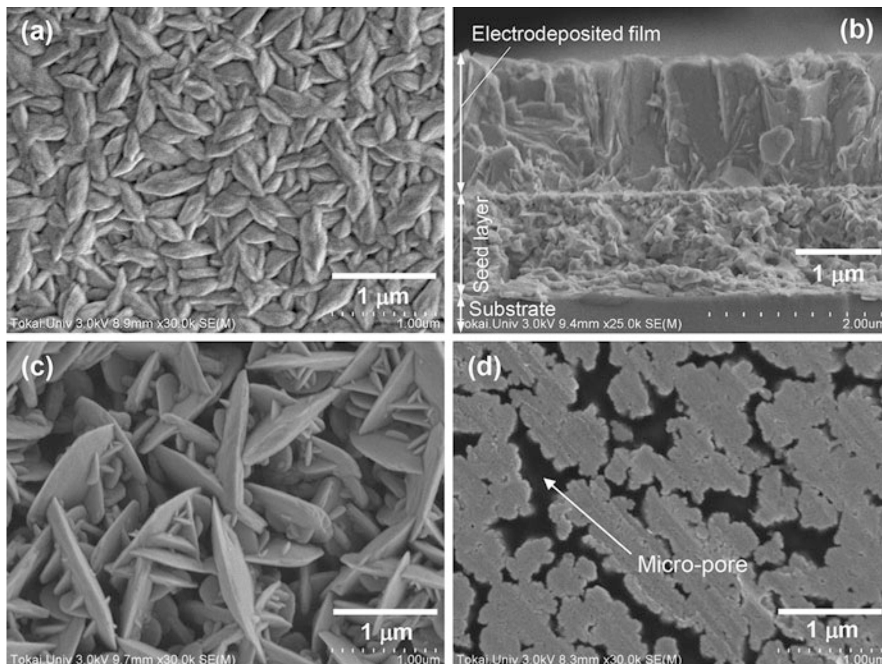

Fig. 1.11 SEM images showing the morphologies of the Bi_2Te_3 films. (**a**, **b**) Surface and cross-section images of the AES film, respectively; (**c**, **d**) top and bottom surface images of the standard electrodeposited film, respectively [58]

film. The top surface image (Fig. 1.11c) shows dendritic growths on the film surface, leading to the rough appearance of the surface. Figure 1.11d shows the bottom surface of the film after detachment from the stainless-steel substrate. A large area of micropores was observed between the crystal grains. Consequently, we attributed the lower electrical conductivity and lower absolute Seebeck coefficient of the standard electrodeposited film to the presence of micropores.

Figure 1.12 shows the in-plane thermoelectric properties of the Bi_2Te_3 films as a function of the applied current density. As a reference, the thermoelectric properties of Bi_2Te_3 films obtained by the standard electrodeposition are also presented in the figure. The reference samples were formed on a stainless-steel substrate using potentiostatic electrodeposition, and subsequently detached from the stainless-steel substrate using epoxy resin. As shown in Fig. 1.12a, the electrical conductivity of the AES film at an applied current density of 1.8 mA/cm^2 was 646 S/cm. When the current density was increased to 2.1 mA/cm^2, the electrical conductivity of the AES film increased, reaching the highest value of 674 S/cm. With the further increase in the current density, the electrical conductivity decreased. The electrical conductivity of the AES film deposited at an applied current density of 2.6 mA/cm^2 was 523 S/cm. The electrical conductivities of the electrodeposited films followed a similar trend with that of the AES films; however, the electrical

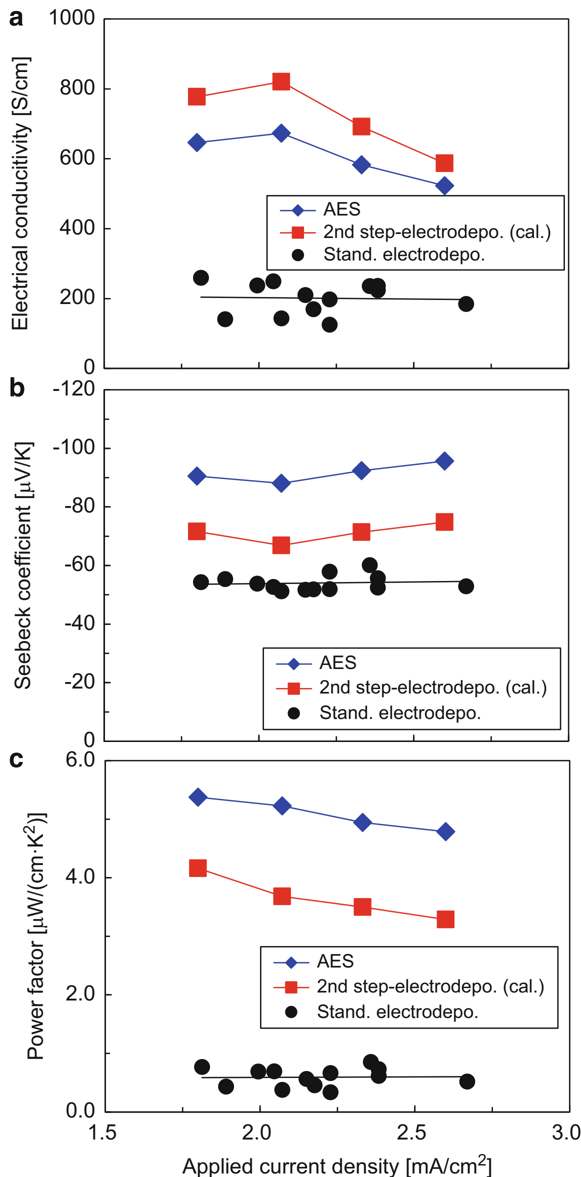

Fig. 1.12 (**a**) Electrical conductivities, (**b**) Seebeck coefficients, and (**c**) power factors of the Bi_2Te_3 films, including the AES film, electrodeposited film, and reference standard electrodeposited film, as a function of the applied current density [58]

conductivity magnitudes of the electrodeposited films were higher than those of the AES films. This indicates that the electrical conductivity of the electrodeposited film was higher than that of the seed layer. The highest value of 821 S/cm was observed for the electrodeposited film obtained at a current density of 2.1 mA/cm^2. Furthermore, the electrical conductivity of the standard electrodeposited film was approximately 200 S/cm, in the range of the applied current density. Therefore,

the electrodeposition using a seed layer contributed to the improvement in the electrical conductivity. Figure 1.12b shows that the Seebeck coefficient of the AES film at an applied current density of 1.8 mA/cm^2 is −91 μV/K. When the current density was increased, the Seebeck coefficient of the AES film did not significantly change. The Seebeck coefficient of the AES film at an applied current density of 2.6 mA/cm^2 was −96 μV/K. To the best of our knowledge, this Seebeck coefficient is significantly higher than the previously reported values. The Seebeck coefficients of the electrodeposited films exhibited a similar trend with that of the AES films. The Seebeck coefficients of the electrodeposited films were in the range of −67 to −75 μV/K. The absolute values were approximately 25% lower than those of the AES films. The standard electrodeposited film exhibited a Seebeck coefficient of approximately −50 μV/K. Therefore, the electrodeposition using the seed layer also improved the Seebeck coefficient. The power factor as a function of the applied current density is shown in Fig. 1.12c. The standard electrodeposited film exhibited a power factor of approximately 0.5 μW/(cm·K^2) within the applied current density range. Moreover, the power factor of the AES film at an applied current density of 1.8 mA/cm^2 was 5.4 μW/(cm·K^2). With the increase in the current density, the power factor of the AES film linearly decreased. For the electrodeposited film, the power factor at an applied current density of 1.8 mA/cm^2 was 4.2 μW/(cm·K^2). With the increase in the current density, the power factor linearly decreased with approximately the same slope as that of the AES films. Overall, the power factors of the electrodeposited films were approximately 15% lower than those of the AES films, indicating that the power factors of the electrodeposited films were lower than that of the seed layer. However, the power factors of the electrodeposited films were 7–9 times higher than that of the standard electrodeposited film. The maximum power factor in this study is comparable to the excellent values of as-grown electrodeposited Bi–Te–Se ternary compounds [59, 60]. In summary, the electrodeposition using the seed layer significantly improved the power factor mainly owing to the increase in the electrical conductivity.

1.2.5 Printing Method

Unlike other film deposition methods such as the dry and wet processes, the printing method uses nanoparticle inks, which are applied to a substrate. This method is the most convenient procedure for the preparation of thin layers with fine patterns. There are mainly two types of printing methods: screen printing and inkjet printing [61–63]. Screen printing is a kind of stencil printing. It is not to print with a plate coated with ink, but to print squeezing ink out of holes made on a plate itself. Inkjet printing is a type of printing that propels drops of ink onto a substrate. One of the important factors in the printing methods is the quality of the ink including thermoelectric nanoparticles. The size and shape of the nanoparticles affect the thermoelectric performance [64–66]. For the analysis of the thermoelectric properties of printed thin films, the drop-cast method is the most appropriate as the thin film can be formed simply by dropping the ink on the substrate and drying it.

The methods for production of nanoparticles can be roughly divided into two types. One of them is a top-down method, in which bulk solids are physically transformed into nanoparticles by pulverization [29, 67]. The other type is a bottom-up method of synthesis of atoms and molecular aggregates (crystals, amorphous particles) through atomic- and molecular-level chemical reactions [68–70].

A common bottom-up synthesis method is ball-milling or bead-milling, based on the most basic crushers used for fine pulverizations of powders and powder raw material particles. Figure 1.13 shows a schematic diagram of the ball-milling method. In this method, the powder material, which should be pulverized, and hard balls, such as metal (stainless steel or tungsten) balls, are placed in a crushing vessel (pot). The pot is placed on the roller of the ball mill equipment and rotates them in the direction of rotation. The raw material powders are pulverized more finely by gradually grinding them by collisions and frictions between the balls in the pot. SEM micrographs of $Bi_{0.4}Te_{3.0}Sb_{1.6}$ nanoparticles fabricated using bead-milling are shown in Fig. 1.14 [32]. The average size of the nanoparticles is approximately 50 nm. The selected area electron diffraction (SAED) pattern of the nanoparticles in Fig. 1.15 shows a dotted structure of diffraction rings with bright spots [29]. This indicates that the nanoparticles exhibit a polycrystalline structure.

We present typical nanoparticle ($Bi_{0.4}Te_{3.0}Sb_{1.6}$) thin films prepared using the drop-casting method [32]. In order to connect the nanoparticles to each other,

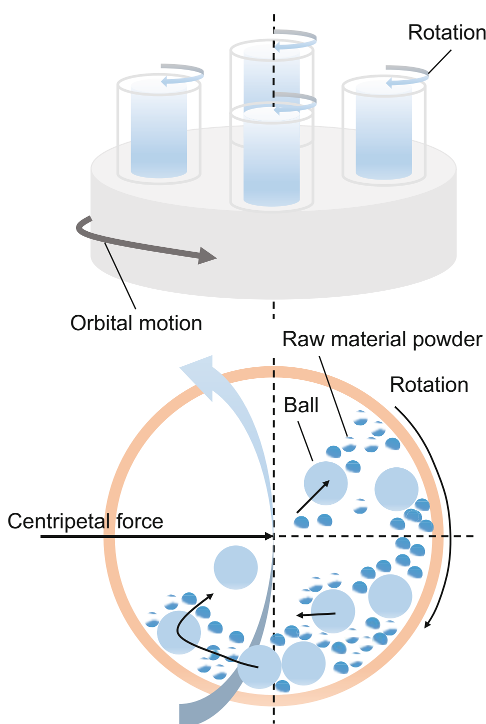

Fig. 1.13 Schematic diagram of the ball-milling method

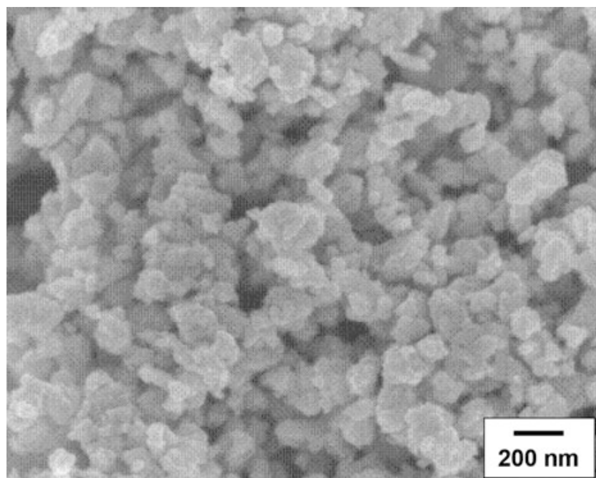

Fig. 1.14 SEM micrograph of the $Bi_{0.4}Te_{3.0}Sb_{1.6}$ nanoparticles [32]

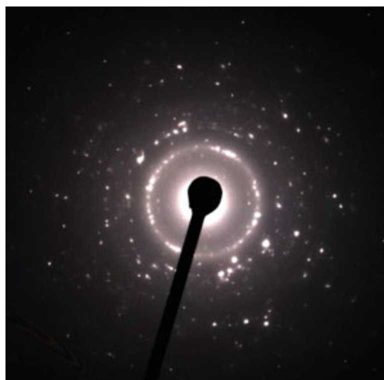

Fig. 1.15 Electron diffraction pattern of the $Bi_{0.4}Te_{3.0}Sb_{1.6}$ nanoparticles [32]

thermal annealing at different temperatures was performed. The cross-section and surface micrographs of the thin films shown in Fig. 1.16 reveal the effects of the annealing temperature. The thin film annealed at 300 °C contains only nanoparticles, which essentially have the same sizes as those in Fig. 1.14. At the annealing temperature of 350 °C, crystal flakes with hexagonal shapes with widths and thicknesses of approximately 500 nm and 50 nm, respectively, were formed on the surface of the thin film. With the further increase in the annealing temperature, the crystal flakes on the surface became larger. The crystal flakes on the nanoparticles exhibited single-crystalline structures [29]. The in-plane thermoelectric properties of the nanoparticle thin films measured at approximately 300 K are shown in Fig. 1.17. At the annealing temperature of 300 °C, the Seebeck coefficient and electrical conductivity of the thin film are 258 μV/K and 1.3 S/cm, respectively. The electrical conductivity is low as the organic components such as

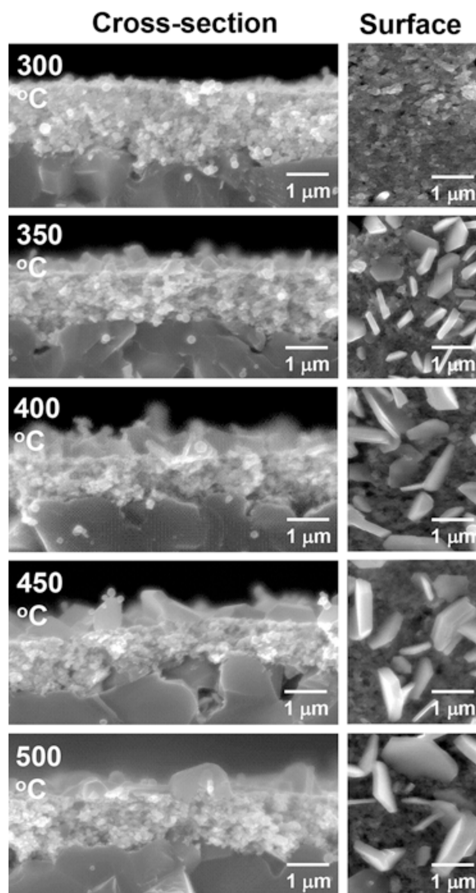

Fig. 1.16 Cross-section and surface SEM micrographs of the $Bi_{0.4}Te_{3.0}Sb_{1.6}$ nanoparticle thin films sintered at various temperatures [32]

the surfactant remain on the surfaces of the nanoparticles so that electrons cannot pass through the surfactant layer between the nanoparticles. With the increase in the annealing temperature, the Seebeck coefficient of the thin film decreased, while the electrical conductivity increased. At an annealing temperature of 500 °C, the Seebeck coefficient and electrical conductivity of the thin film are 65 μV/K and 109 S/cm, respectively. The highest achieved thermoelectric power factor is 1.3 μW/(cm·K^2) at an annealing temperature of 350 °C. Compared to that of the bulk material, the thermoelectric power factors of the nanoparticle thin films are low. In order to further improve the thermoelectric properties of the nanoparticle thin films, it is necessary to investigate in detail the origin of the degraded thermoelectric properties.

The bottom-up synthesis method generally utilizes a homogeneous nucleation followed by a solid-phase precipitation. For the synthesis of thermoelectric nanoparticles including nanoplates, nanosheets, nanorods, etc., liquid-phase methods (hydrothermal method, liquid-phase precipitation method, and electro-chemical synthesis), gas-phase methods (chemical vapor deposition and chemical

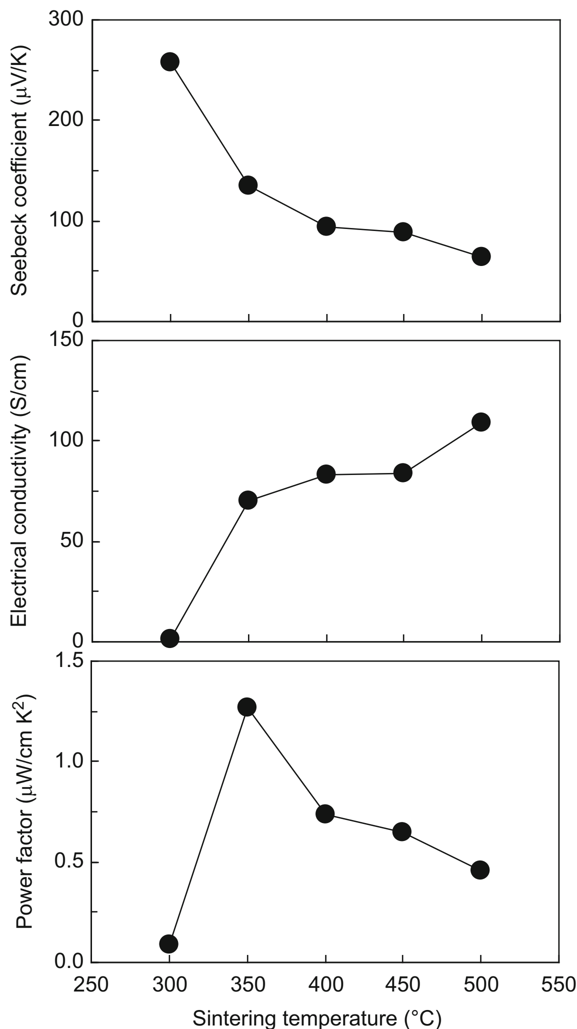

Fig. 1.17 In-plane Seebeck coefficients, electrical conductivities, and thermoelectric power factors of the $Bi_{0.4}Te_{3.0}Sb_{1.6}$ nanoparticle thin films as a function of the annealing temperature [32]

vapor transport), and solid-phase method (spinodal decomposition method) are commonly employed [71–73]. Among them, the hydrothermal method can be used to effectively fabricate nanoscale single-crystals, which are very favorable for a thermoelectric performance improvement. Therefore, the hydrothermal synthesis will be described below as a typical example of a bottom-up synthesis method.

The hydrothermal synthesis is a synthesis or crystal growth of a compound performed in the presence of hot water at high temperature and pressure. As substances insoluble in water are easily dissolved at normal temperature and pressure, it is possible to synthesize and grow substances that normally cannot be obtained. In particular, a hydrothermal synthesis method using an organic solvent instead of hot water is referred to as solvothermal method. In the bismuth tellurium

system, it is common to use the solvothermal method. Figure 1.18 shows a schematic diagram of the hydrothermal synthesis. The starting material and water (organic solvent) are usually placed in a sealed container (autoclave); the container is sealed and heated to obtain the product. After the synthesis, the products are naturally cooled down to room temperature. The products were collected using centrifugation and were washed several times in distilled water and absolute methanol. Finally, they were dried in vacuum at a temperature lower than 100 °C for approximately 24 h. A transmission electron microscope (TEM) image of a typical Bi_2Te_3 nanoplate synthesized using the solvothermal method is shown in Fig. 1.19 [66]. The shape of the nanoplate is a regular hexagon, whose surface is significantly flattened. The edge size of the nanoplate was approximately 900 nm and the thickness was expected to be very small (smaller than 50 nm) as the mesh structure behind the nanoplate can be observed. The SAED pattern shown in the inset of Fig. 1.19 was obtained from the tip of the hexagonal nanoplate. The hexagonally

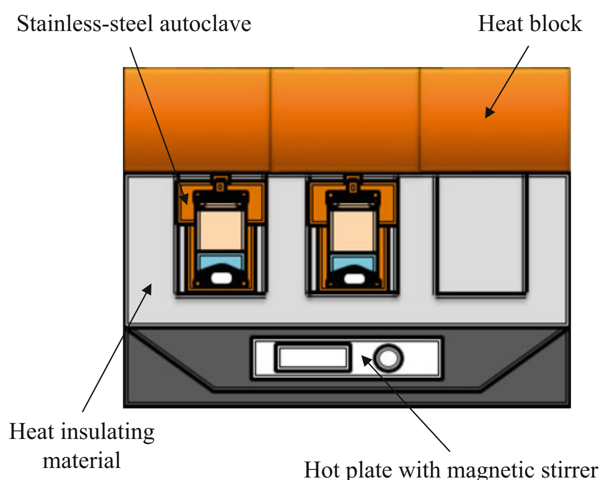

Fig. 1.18 Schematic diagram of the hydrothermal synthesis [31]

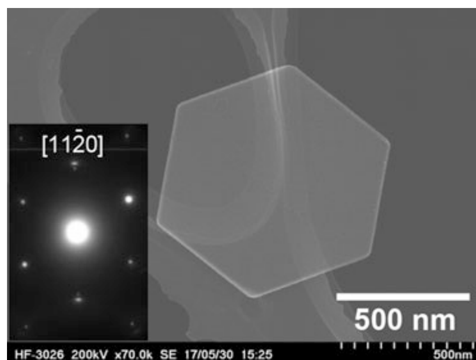

Fig. 1.19 TEM image of a Bi_2Te_3 nanoplate prepared by a solvothermal synthesis. The inset shows the corresponding SAED pattern [66]

symmetric spot pattern indicated single crystallinity and can be indexed on the basis of a rhombohedral cell. Briefly, the mechanism of crystal growth of Bi_2Te_3 nanoplates is as follows. Once the Bi_2Te_3 nuclei were generated by the chemical reactions, they aggregated. When the radius of the aggregated nuclei became larger than that of their critical nucleus, Bi_2Te_3 nanoparticles were generated. The formation of the nanoplate was also attributed to the inherent crystal structure. Owing to the high surface energy of the nuclei, the aggregated Bi_2Te_3 particles were not in thermodynamic equilibrium and were metastable; therefore, Bi_2Te_3 nanoplates with better crystallinities became thermodynamically preferred. After the formation of Bi_2Te_3 nanoplates, the Ostwald ripening process proceeded. The smaller nanoparticles adsorbed around plates were consumed and grew gradually leading to larger nanoplates along the top–bottom crystalline plane. This occurred as the rhombohedral Bi_2Te_3 can be described as a stack of infinite layers extending along the top–bottom crystalline plane connected by van der Waals bonds, as shown in Fig. 1.1. From a thermodynamic perspective, the free energy of a broken covalent bond is higher than that of a dangling van der Waals bond. This implies that the Bi_2Te_3 crystal growth along the top–bottom crystalline plane should be significantly faster than that along the *c*-axis, which is perpendicular to the top–bottom planes, as the crystalline facets tend to develop on the low-index plane.

Typical nanoplate (Bi_2Te_3) thin films were prepared using the drop-casting method [66]. In order to connect the nanoplates to each other, thermal annealing at different temperatures was performed. Cross-section and surface micrographs of the as-prepared thin film are shown in Fig. 1.20. The surface image in Fig. 1.20a shows that the thin film is composed of high-purity hexagonal nanoplates with edge sizes in the range of 500–2000 nm (average size of 1000 nm). The hexagonal nanoplates were well aligned in the direction of the film surface, but some apertures were observed in the thin film. A cross-sectional image of the nanoplate thin film is shown in Fig. 1.20b. The hexagonal Bi_2Te_3 nanoplates were well piled up; the approximate thickness of the thin film was 40 μm. Figure 1.21 shows SEM images of the surface morphologies of the Bi_2Te_3 nanoplate thin films obtained at different

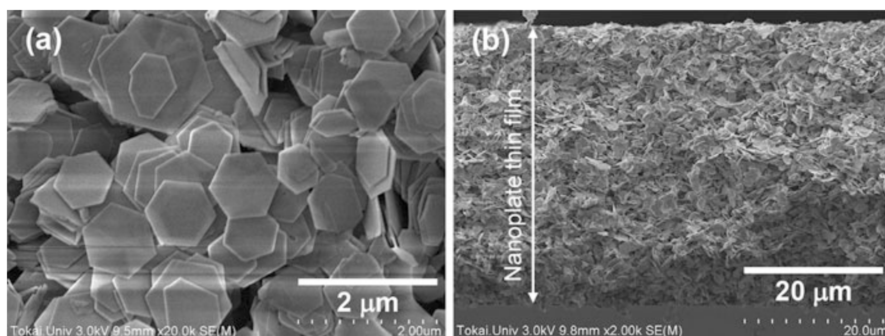

Fig. 1.20 (**a**) Surface and (**b**) cross-sectional morphologies of an untreated Bi_2Te_3 nanoplate thin film, observed by SEM [66]

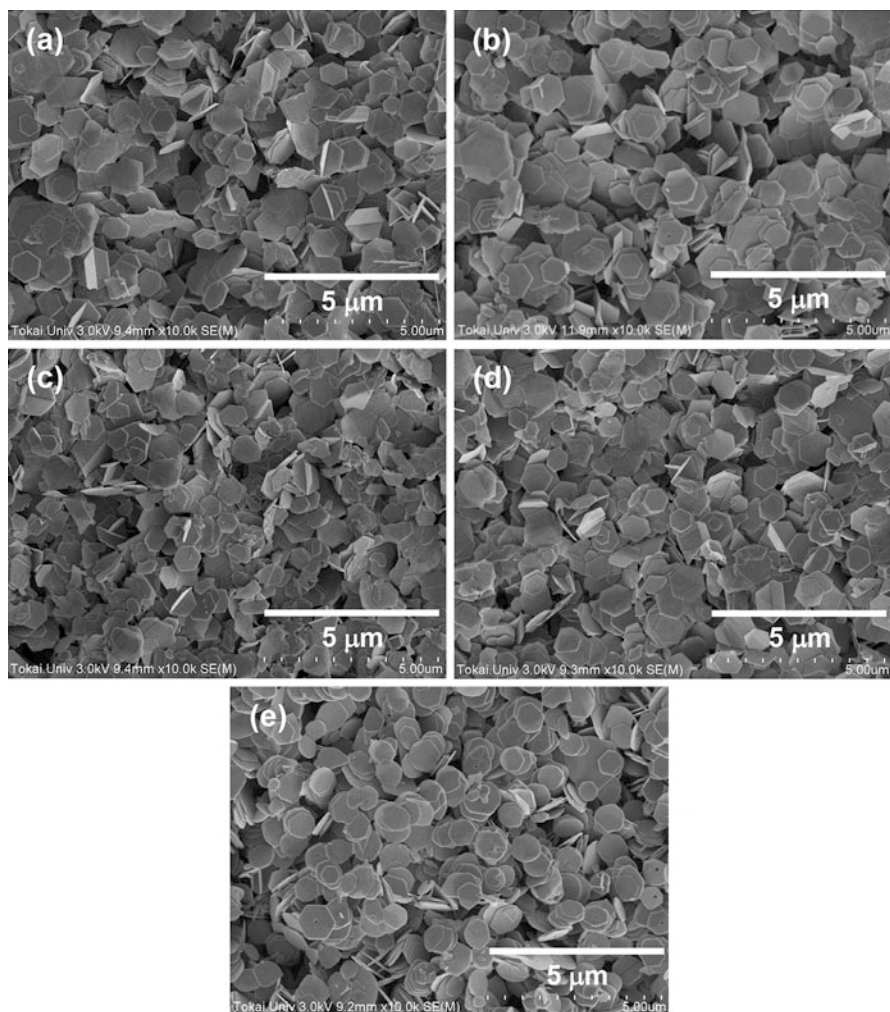

Fig. 1.21 SEM images of the surface morphologies of the Bi_2Te_3 nanoplate thin films annealed at (**a**) 200, (**b**) 250, (**c**) 300, (**d**) 350, and (**e**) 400 °C [66]

annealing temperatures. Overall, in all of the Bi_2Te_3 nanoplate thin films obtained at annealing temperatures of 200–400 °C, high-purity nanoplates were well aligned in the direction of the film surface. In terms of fine structure, the nanoplate thin films annealed at 200 and 250 °C clearly exhibited the edges of the hexagonal nanoplates (Figs. 1.21a, b). However, with the increase in the annealing temperature to 300 and 350 °C, the edges of the hexagonal nanoplates gradually disappeared (Figs. 1.21c, d). The shape of the nanoplates annealed at 400 °C was not hexagonal, but circular (Fig. 1.21e), as Bi or Te atoms at the edges of the hexagonal nanoplates evaporated during the thermal annealing at the higher temperature.

The in-plane thermoelectric properties of the nanoplate thin films measured at approximately 300 K are shown in Fig. 1.22. The thermoelectric properties of two samples, untreated thin film and thin film annealed at 200 °C, are not included in Fig. 1.22 as their electrical resistivities were too high so that the thermoelectric properties could not be measured. This indicates that the nanoplates did not tightly join with each other when the annealing temperature was smaller than 200 °C.

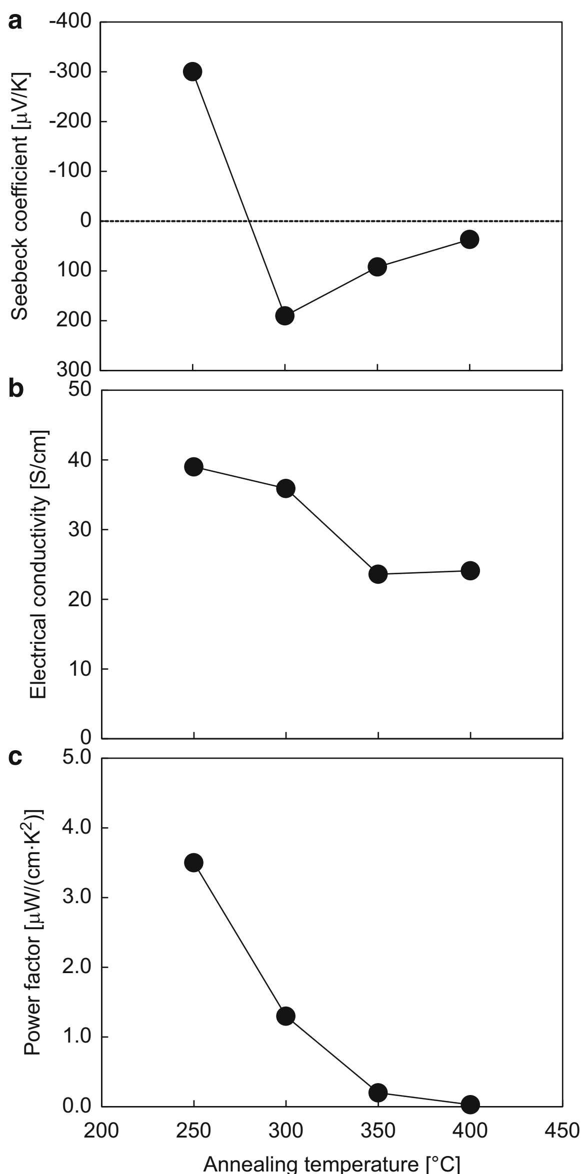

Fig. 1.22 In-plane thermoelectric properties of the Bi_2Te_3 nanoplate thin films as a function of the annealing temperature. (**a**) Seebeck coefficient, (**b**) electrical conductivity, and (**c**) power factor [66]

Figure 1.22a shows that the Seebeck coefficient of the nanoplate thin film annealed at 250 °C was −300 μV/K, higher than those reported for Bi_2Te_3 materials [6]. With the increase in the annealing temperature, the Seebeck coefficient became positive. The nanoplate thin film annealed at 300 °C exhibited a Seebeck coefficient of 190 μV/K. With the increase in the annealing temperature, the Seebeck coefficients of the nanoplate thin films approached the value of zero. This occurred as the atomic composition of the thin film was different from the stoichiometric composition owing to the partial atomic evaporation. Figure 1.22b shows that the electrical conductivity of the nanoplate thin film annealed at 250 °C was 39 S/cm, which is the highest value in this study. This indicates that the contact between nanoplates was enhanced by the thermal annealing. The annealing temperature dependence of the power factor of the nanoplate thin films is shown in Fig. 1.22c. The power factor of the nanoplate thin film rapidly decreased with the increase in the annealing temperature. The maximum power factor of 3.5 μW/(cm·K^2) was obtained at the annealing temperature of 250 °C.

1.3 Thin-Film Thermoelectric Generators

Typical thin-film thermoelectric generators prepared by RF magnetron sputtering are presented in this section. The fabrication process of the multi-layered thermoelectric generator is illustrated in Fig. 1.23 [3]. Initially, we prepared a glass substrate (Eagle XG, Corning) (20 × 30 mm^2; thickness: 0.3 mm), thinner than that used in the experiments to understand the optimal conditions for thermal annealing, for fabrication of as thin as possible generators. A p-type Sb_2Te_3 film with a thickness of 1.0 mm was deposited on one side of the glass substrate, and an n-type film with a thickness of 1.0 mm was sequentially deposited on the other side of the substrate by RF magnetron sputtering. Following the film deposition, a thermal annealing was carried out at the optimal temperature. The p-type film was then connected with the n-type film by spraying silver paste at the one-side edge face of the substrate. After baking the sample to dry the silver paste, the sample was wrapped with an insulation tape, except the part of the opposite edge side of the sample on which silver paste was not sprayed (step 3). Silver paste was then sprayed on the unwrapped positions of both p-Sb_2Te_3 and n-Bi_2Te_3 films (step 4). In the next step (step 5), a piece of the obtained sample was connected with others as p–n junctions connected in series. In step 6, 11 pieces of samples were connected in series followed by baking of the samples to connect each piece of the sample tightly. Finally, the multi-layered sample was bundled by wrapping the insulation tape. A cross-section photograph of the obtained multi-layered thermoelectric generator shows that the total thickness of the generator is ~7 mm, and that there are no clear gaps between the pieces.

A photograph of the measurement system of the multi-layered thermoelectric generator is shown in Fig. 1.24a. In order to achieve a temperature difference between the ends of the generator, the lower half of the generator was dipped in hot

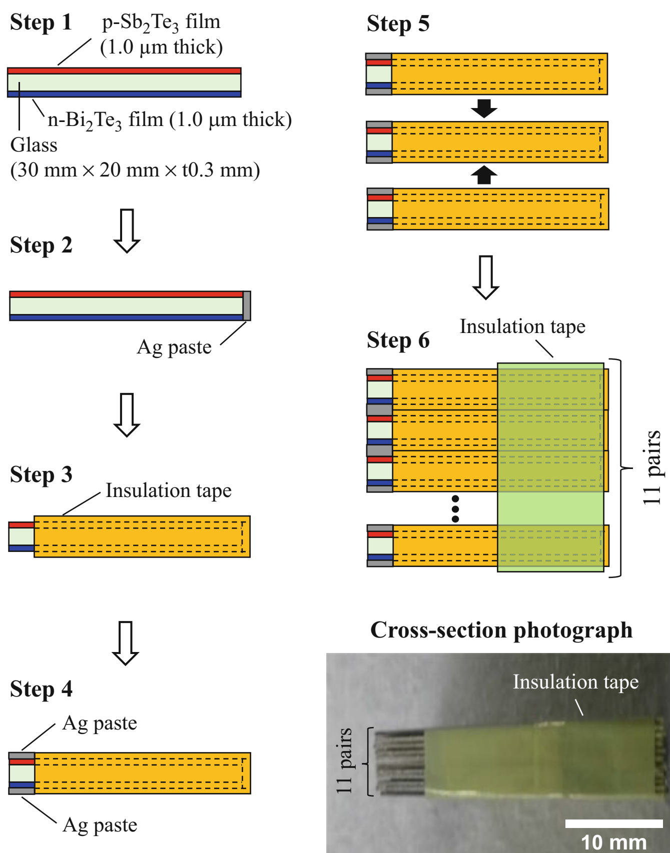

Fig. 1.23 Fabrication process of the multi-layered thermoelectric generator [3]

water, while the upper half was maintained in the atmosphere. The temperatures on both sides were monitored using thermocouples (K-type) attached on the generator. Two electrodes were connected to the Bi_2Te_3 and Sb_2Te_3 sides of the substrate. The temperature difference was generated by changing the temperature of the hot water; the open-circuit voltage (V_{oc}) was measured using a digital multimeter. The performance of the multi-layered thermoelectric generator as a function of the temperature difference is shown in Fig. 1.24b. The temperature difference at the ends was changed from 11 to 28 K. At a temperature difference of 11 K, V_{oc} of 23.7 mV was achieved. With the increase in the temperature difference, V_{oc} linearly increased. V_{oc} of 32.0 mV was achieved at a temperature difference of 28 K. Our results were in relatively good agreement with those in previous studies with similar device structures and temperature differences [74–76]. The maximum output power ($P_{\max}$) is expressed as: $P_{\max} = V_{oc}^2/4R_{\text{total}}$, where R_{total} is the measured total resistance of the multi-layered thermoelectric generator, which mainly comprises

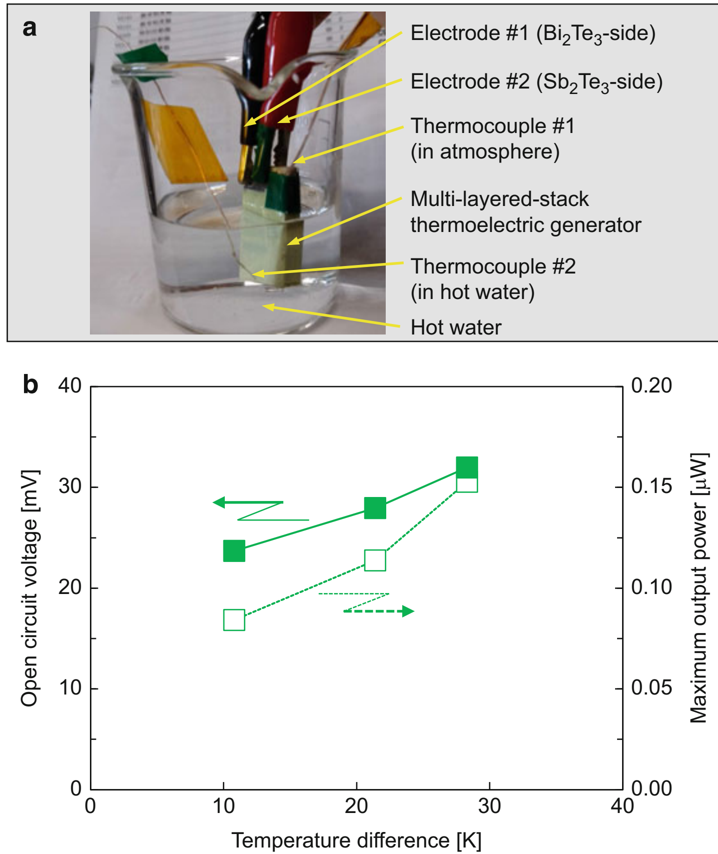

Fig. 1.24 (**a**) Photograph of the measurement system of the multi-layered thermoelectric generator. (**b**) Open-circuit voltages and maximum output powers of the multi-layered thermoelectric generator at various temperature differences [3]

the resistances of the p- and n-type thin films, R_{film}, and contact resistance, R_c. R_{total} of the generator measured using a digital multimeter was 1.6 kΩ. P_{max} was estimated to be 0.08 μW at the temperature difference of 11 K. P_{max} increased with the temperature difference; P_{max} of 0.15 μW was achieved at the temperature difference of 28 K.

1.4 Summary

In this chapter, the crystal structures of Bi_2Te_3-based alloys were presented. An overview of thin-film deposition methods was also presented, and typical conventional deposition methods such as sputtering, electrodeposition, and printing

were introduced using typical experimental results of Bi_2Te_3-based alloy thin films. As the presented film fabrication methods have distinct characteristics, the film fabrication method should be selected according to the application. Finally, a typical thin-film thermoelectric generator, consisting of a multi-layered structure of p-type Sb_2Te_3 and n-type Bi_2Te_3 thin films, was introduced. Bi_2Te_3-based alloys are relatively old thermoelectric materials whose research and development began in the 1950s. However, the material properties have been improved using the latest thin-film process technologies by nanostructuring, which makes this research field very attractive with significant potentials for novel findings.

References

1. A. Kadhim, A. Hmood, H. Abu Hassan, Mater. Lett. **97**, 24 (2013)
2. Y. Ito, M. Mizoshiri, M. Mikami, T. Kondo, J. Sakurai, S. Hata, Jpn. J. Appl. Phys. **56**, 06GN06 (2017)
3. K. Takayama, M. Takashiri, Vacuum **144**, 164 (2017)
4. H. Yamamuro, N. Hatsuta, M. Wachi, Y. Takei, M. Takashiri, Coatings **8**, 22 (2018)
5. J.H. Goldsmid, *Materials Used in Semiconductor Devices* (Wiley, New York, 1965)
6. H. Scherrer, S. Scherrer, in *CRC Handbook of Thermoelectrics*, ed. by D. M. Rowe, (CRC Press, Boca Raton, 1995), p. 211
7. H. Kaibe, Y. Tanaka, M. Sakata, I. Nishida, J. Phys. Chem. Solids **50**, 945 (1989)
8. P.J. Taylor, J.R. Maddux, W.A. Jesser, F.D. Rosi, J. Appl. Phys. **85**, 7807 (1999)
9. K. Yamauchi, M. Takashiri, J. Alloys Compd. **698**, 977 (2017)
10. S. Kudo, S. Tanaka, K. Miyazaki, Y. Nishi, M. Takashiri, Mater. Trans. **58**, 513 (2017)
11. G.S. Nolas, J. Sharp, H.J. Goldsmid, *Thermoelectrics* (Springer, New York, 2001)
12. W.M. Yim, F.D. Rosi, Solid State Electron. **15**, 1121 (1972)
13. M. Takashiri, K. Imai, M. Uyama, H. Hagino, S. Tanaka, K. Miyazaki, Y. Nishi, J. Appl. Phys. **115**, 214311 (2014)
14. T. Inamoto, M. Takashiri, J. Appl. Phys. **120**, 125105 (2016)
15. S.K. Mishra, S. Satpathy, O. Jepsen, J. Phys. Condens. Matter **9**, 461 (1997)
16. X. Luo, M.B. Sullivan, S.Y. Quek, Phys. Rev. B Condens. Matter **86**, 184111 (2012)
17. G. Wang, T. Cagin, Phys. Rev. B Condens. Matter **76**, 075201 (2007)
18. K. Yildiz, U. Akgul, H.S. Leipner, Y. Atic, Superlattice. Microst. **58**, 2013 (2013)
19. D. Bourgault, C.G. Garampon, N. Caillault, L. Carbone, J.A. Aymami, Thin Solid Films **516**, 8579 (2008)
20. K. Kusagaya, M. Takashiri, J. Alloys Compd. **653**, 480 (2015)
21. X. Duan, Y. Jiang, Appl. Surf. Sci. **256**, 7365 (2010)
22. A.J. Zhou, L.D. Feng, H.G. Cui, J.Z. Li, G.Y. Jiang, X.B. Zhao, J. Electron. Mater. **42**, 2184 (2013)
23. M. Takashiri, K. Kurita, H. Hagino, S. Tanaka, K. Miyazaki, J. Appl. Phys. **118**, 065301 (2015)
24. M. Uchino, K. Kato, H. Hagino, K. Miyazaki, J. Electron. Mater. **42**, 1814 (2012)
25. J. Kuleshova, E. Koukharenko, X. Li, N. Frety, S. Nandhakumar, J. Tudor, S.P. Beeby, N.M. White, Langmuir **26**, 16980 (2010)
26. K. Matsuoka, M. Okuhata, N. Hatsuta, M. Takashiri, Trans. Mater. Res. Soc. Jpn **40**, 373 (2015)
27. K. Matsuoka, M. Okuhata, M. Takashiri, J. Alloys Compd. **649**, 721 (2015)
28. C.V. Manzano, B. Abad, M.M. Rojo, Y.R. Koh, S.L. Hodson, A.M.L. Martinez, X. Xu, A. Shakouri, T.D. Sands, T. Borca-Tasciuc, M. Martin-Gonzalez, Sci. Rep. **6**, 19129 (2016)
29. M. Takashiri, S. Tanaka, K. Miyazaki, J. Cryst. Growth **372**, 199 (2013)

30. M. Koyano, S. Mizutani, Y. Hayashi, S. Nishino, M. Miyata, T. Tanaka, K. Fukuda, J. Electron. Mater. **46**, 2873 (2017)
31. K. Wada, K. Tomita, M. Takashiri, J. Cryst. Growth **468**, 194 (2017)
32. M. Takashiri, S. Tanaka, M. Takiishi, M. Kihara, K. Miyazaki, H. Tsukamoto, J. Alloys Compd. **462**, 351 (2008)
33. R.S. Makala, K. Jagannadham, B.C. Sales, J. Appl. Phys. **94**, 3907 (2003)
34. H. Obara, S. Higomo, M. Ohta, A. Yamamoto, K. Ueno, T. Iida, Jpn. J. Appl. Phys. **48**, 085506 (2009)
35. P.H. Le, C.N. Liao, C.W. Luo, J. Leu, J. Alloys Compd. **615**, 546 (2014)
36. L. Thi, C. Tuyen, P. Huu, L. Chih, W. Luo, J. Leu, J. Alloys Compd. **673**, 107 (2016)
37. A. Al Bayaz, A. Giani, M.C. Artaud, A. Foucaran, F. Pascal-Delannoy, A. Boyer, J. Cryst. Growth **241**, 463 (2002)
38. H.W. You, S.-H. Bae, J. Kim, J.-S. Kim, C. Park, J. Electron. Mater. **40**, 635 (2011)
39. R. Venkatasubramanian, T. Colpitts, E. Watko, M. Lamvik, N. El-Masry, J. Cryst. Growth **170**, 817 (1997)
40. Y. Kim, A. DiVenere, G.K.L. Wong, J.B. Ketterson, S. Cho, J.R. Meyer, J. Appl. Phys. **91**, 716 (2002)
41. Z. Wang, X. Zhang, Z. Zeng, Z. Zhang, Z. Hua, ECS Electrochem. Lett. **3**, 99 (2014)
42. X. Zhang, Z. Zeng, C. Shen, Z. Zhang, Z. Wang, J. Appl. Phys. **115**, 024307 (2014)
43. K. Zhang, F. Zhu, C.H.A. Huan, A.T.S. Wee, Thin Solid Films **376**, 255 (2000)
44. S. Ishibashi, Y. Higuchi, Y. Ota, J. Vac. Sci. Technol. A **8**, 1399 (1990)
45. K. Zhang, F. Zhu, C.H.A. Huan, A.T.S. Wee, J. Appl. Phys. **86**, 974 (1999)
46. J.-L. Chung, J.-C. Chen, C.-J. Tseng, Appl. Surf. Sci. **255**, 2494 (2008)
47. M. Takashiri, K. Takano, J. Hamada, Thin Solid Films **664**, 100 (2018)
48. M. Takashiri, T. Shirakawa, K. Miyazaki, H. Tsukamoto, Trans. Jpn. Soc. Mech. Eng. Ser. **72**, 1793 (2006)
49. G. Yuan, Y. Li, N. Bao, J. Miao, C. Ge, Y. Wang, Mater. Chem. Phys. **143**, 587 (2014)
50. J.W.G. Bos, H.W. Zandbergen, M.-H. Lee, N.P. Ong, R.J. Cava, Phys. Rev. B **75**, 195203 (2007)
51. Y. Horio, A. Inoue, Mater. Trans. JIM **47**, 1412 (2006)
52. L.D. Zhao, B.-P. Zhang, W.S. Liu, H.L. Zhang, J.-F. Li, J. Alloys Compd. **467**, 91 (2009)
53. Q. Lognone, F. Gascoin, J. Alloys Compd. **610**, 1 (2014)
54. M. Takashiri, T. Shirakawa, K. Miyazaki, H. Tsukamoto, J. Alloys Compd. **441**, 246 (2007)
55. H. Huang, W. Luan, S. Tu, Thin Solid Films **517**, 3731 (2009)
56. M. Takahashi, Y. Katou, K. Nagata, S. Furuta, Thin Solid Films **240**, 70 (1994)
57. N. Hatsuta, D. Takemori, M. Takashiri, J. Alloys Compd. **685**, 147 (2016)
58. M. Takashiri, T. Makioka, H. Yamamuro, J. Alloys Compd. **764**, 802 (2018)
59. S. Michel, S. Diliberto, N. Stein, B. Bolle, C. Boulanger, J. Solid State Electrochem. **12**, 95 (2008)
60. C. Schumacher, K.G. Reinsberg, R. Rostek, L. Akinsinde, S. Baessler, S. Zastrow, G. Rampelberg, P. Woias, C. Detavernier, J.A.C. Broekaert, J. Bachann, K. Nielsch, Adv. Energy Mater. **3**, 95 (2013)
61. B. Vermeersch, J.-H. Bahk, J. Christofferson, A. Shakouri, J. Alloys Compd. **582**, 177 (2014)
62. C. Navone, M. Soulier, M. Plissonnier, A.L. Seiler, J. Electron. Mater. **39**, 1755 (2010)
63. H.Q. Liu, X.B. Zhao, T.J. Zhu, Y. Song, F.P. Wang, Curr. Appl. Phys. **9**, 409 (2009)
64. M. Zebarjadi, K. Esfarjani, A. Shakouri, Z. Bian, J.-H. Bahk, G. Zeng, J. Bowers, H. Lu, J. Zide, A. Gossard, J. Electron. Mater. **39**, 1755 (2010)
65. Q. Zhang, X. Ai, L. Wang, Y. Chang, W. Luo, W. Jiang, L. Chen, Adv. Funct. Mater. **25**, 966 (2015)
66. Y. Hosokawa, K. Wada, M. Tanaka, K. Tomita, M. Takashiri, Jpn. J. Appl. Phys. **57**, 02CC02 (2018)
67. M. Toprak, Y. Zhang, M. Muhammed, Mater. Lett. **57**, 3976 (2003)
68. F.-J. Fan, Y.-X. Wang, X.-J. Liu, L. Wu, S.-H. Yu, Adv. Mater. **24**, 6158 (2011)
69. Y. Zhao, J.S. Dyck, B.M. Hernandez, C. Burda, J. Phys. Chem. C **114**, 11607 (2010)

70. J.S. Son, M.K. Choi, M.-K. Han, K. Park, J.-Y. Kim, S.J. Lim, M. Oh, Y. Kuk, C. Park, S.-J. Kim, T. Hyeon, Nano Lett. **12**, 640 (2012)
71. H.T. Zhang, X.G. Luo, C.H. Wang, Y.M. Xiong, S.Y. Li, X.H. Chen, J. Cryst. Growth **265**, 558 (2004)
72. C. Chen, Z. Ding, Q. Tan, H. Qi, Y. He, Powder Technol. **257**, 83 (2014)
73. A.I. Hochbaum, R. Chen, R.D. Delgado, W. Liang, E.C. Garnett, M. Najarian, A. Majumdar, P. Yang, Nature **451**, 163 (2008)
74. M. Takashiri, T. Shirakawa, K. Miyazaki, H. Tsukamoto, Int. J. Transp. Phenom. **9**, 261 (2007)
75. M. Mizoshiri, M. Mikami, K. Ozaki, Jpn. J. Appl. Phys. **52**, 06GL07 (2013)
76. P. Fan, Z.-H. Zheng, Z.-K. Cai, T.-B. Chen, P.-J. Liu, X.-M. Cai, D.-P. Zhang, G.-X. Liang, J.-T. Luo, Appl. Phys. Lett. **102**, 033904 (2013)